Lattice Boltzmann Simulation of the ETW Slotted Wall Test Section

Benedikt König and Ehab Fares
Exa GmbH
Curiestrasse 4, 70563 Stuttgart, GERMANY

benedikt@exa.com, ehab@exa.com

Martin C.N. Wright
European Transonic Windtunnel GmbH
Ernst-Mach-Strasse 51147 Köln, GERMANY

mcw@etw.de

ABSTRACT

Unsteady transonic Lattice Boltzmann simulations of the NASA Common Research Model in the European Transonic Windtunnel are presented. Modelling of the slotted wall transonic test section is described and different simulation approaches are discussed. Quantitative comparisons are performed using data obtained for the NASA Common Research Model at its design point and at off-design conditions. Good qualitative and quantitative agreement between simulations and uncorrected experimental measurements are shown.

1.0 INTRODUCTION

The present corrections applied at the European Transonic Windtunnel (ETW) have been derived from a comparison of test data acquired for a model tested in the slotted test section with fully test data acquired for the same model tested in the solid test section with corrections derived with a simplified wall interference method based on wall signatures. Although the wall interference corrections have been derived for a specific transport model a generalization of the formulae based on model sizing criteria allows for a wider range of application for similar models.

The present study aims to evaluate the corrections for the NASA Common Research Model (NASA-CRM) at the design condition close to Mach 0.85 and at a cruise lift coefficient, and also at test conditions close to the envelope limits where buffet onset is already encountered and the model characteristics include significant areas of separated flow. The study aims to demonstrate that the test section, plenum, and slot flow can be modelled in sufficient detail to enable the wall signatures to be predicted with sufficient confidence. The ability of the flow simulation to achieve this aim is a prerequisite to deriving wall interference corrections for ETW's slotted wall test section by comparing the modelled characteristics with the corresponding free air simulation.

Providing the simulation in the slotted wind tunnel can be validated, it can then be applied in a more general form to derive wall interference corrections for a more extensive range of test conditions than those currently available. However, the numerical simulation of ventilated test sections as used for transonic wind tunnel testing is still a challenging task for today's CFD methods. The cryogenic ETW, as the leading wind tunnel for testing aircraft at real-flight conditions, features slotted walls, connecting the inside of the test section to a surrounding plenum. Flow can leave and enter the test section to eliminate chocking at near-sonic flow conditions. Consequently, there is a large spread of the velocity scales encountered, ranging from locally supersonic speeds inside the test section to very slow flow inside the plenum chamber. This can be challenging for many simulation tools adapted to either low- or high-speed flows. Another problem often faced when trying to numerically simulate such a test section is the geometrical complexity. While grid generation for simplified

slot geometries may be feasible, it quickly becomes a labour-intensive task when a complex test article inside a realistic wind tunnel geometry is considered.

In the past, several efforts were undertaken to investigate wall interferences in ventilated test sections by means of CFD. In most cases, the wall openings were not actually resolved by the simulation but modelled using various types of porous wall boundary conditions [1, 2, 3]. One of the obvious limitations of this approach is the assumption of well defined, or even constant, conditions inside the slots and the plenum chamber around the test section. This assumption, however, may not be valid for large models or for flow conditions, which induce relatively strong gradients in the flow properties close to the wind tunnel walls. Some results where the slots and the plenum were included in the simulations have been published by Maseland et al [4] for the DNW-HST and, in particular, by Kursakov et al for the ETW [5].

The work presented here is based on a transonic Lattice Boltzmann method (LBM). LBM itself is considered a novel, non-traditional CFD technique [6] that offers several valuable capabilities beyond the classical Navier-Stokes based methods. A transonic extension of the standard LBM, as implemented in the commercial PowerFLOW code, now removes the limitation of the original method to low subsonic flows. Some of the most interesting features of this method for the current application include the capabilities to automatically mesh arbitrarily complex geometries and to handle the different velocity scales with low numerical dissipation.

2.0 DESCRIPTION OF THE ETW

The European Transonic Windtunnel (ETW) is a cryogenic, Göttingen-type tunnel with slotted walls with an adaptive permeability of 0-7.4%. Its Mach number range is from 0.15 to 1.35, covering Reynolds numbers up to 50 million for full models and 90 million for half-models. Independent variation of temperature and pressure thereby allows to separate pure Reynolds number effects from aeroelastic effects. Flow temperature (110-313 K) and total pressure (1.1-4.5 bar) are controlled by injection of liquid nitrogen and exhaust of gaseous nitrogen.

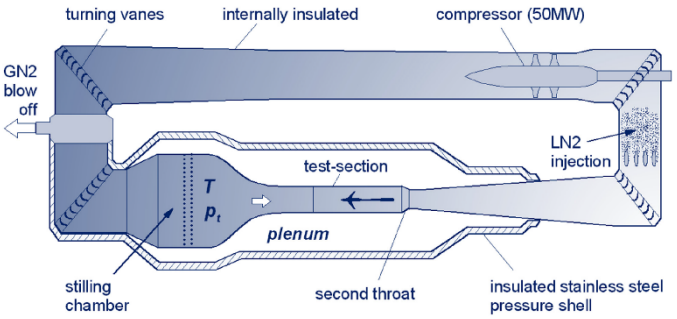

Figure 2-1: Illustration of the ETW aerodynamic circuit

An extensive set of corrections covering all types of models and model/sting combinations have been worked out [7]. Those corrections include residual pressure gradients, buoyancy effects, wall interferences, effects of flow angularity and curvature, and base pressure corrections to the balance forces.

3.0 NUMERICAL METHOD

3.1 Lattice Boltzmann Method

The numerical simulations were performed using the transonic capability of PowerFLOW®, version 5.4b, a flow solver based on extensions of the Lattice Boltzmann model (LBM) [8], developed and distributed by Exa. LBM is a CFD technology developed over the last 30 years [9, 10, 11, 12, 13]. It has been extensively validated for a wide variety of applications ranging from academic direct numerical simulation (DNS) cases [14] to industrial flow problems in the fields of aerodynamics [15, 16] and aeroacoustics [17, 18, 19]. LBM has long been restricted to low compressible isothermal flows. Recent developments based on the scientific research documented in References [20, 21, 22, 23], and similar to what was described by Fares et al [24], enabled the extension of the local Mach number regime up to $M \approx 2$, including shock discontinuities and consistent

compressible gas dynamics. The explicit unsteady nature of the solution makes the code especially well-suited for problems involving separated flows, shock movements and shock boundary layer interaction. The new code extensions still rely on the mesoscopic description of the flow and retain the benefits of the LBM formulation, like for example a highly efficient local implementation of the algorithm suitable for scalable distributed computations on thousands of processors.

3.1.1 Turbulence Modelling

The Lattice Boltzmann flow simulation is equivalent to a DNS of the flow. For high Reynolds number (Re) flows, such as those addressed in this work, the Lattice Boltzmann Very Large Eddy Simulation (LB-VLES) approach described in References [25, 10, 26] is used. It is conceptually similar to hybrid RANS/LES methods, like for example the Scale Adaptive Simulation [27], where especially turbulent high Re boundary layers are modelled but large vortical structures are resolved.

3.1.2 Wall Treatment

The Lattice Boltzmann bounce-back boundary condition for no-slip or the specular reflection for free-slip condition are generalized through a volumetric formulation [9, 28] near the wall for arbitrarily oriented surface elements (surfels) within the Cartesian volume elements (voxels). This formulation of the boundary condition on a curved surface cutting the Cartesian grid is automatically mass, momentum, and energy conservative, while maintaining the spatial order of accuracy of the underlying LBM numerical scheme. To reduce the resolution requirements near the wall for high Re flows, a hybrid wall function is used to model the region of the boundary layer closest to the solid surfaces [29] including compressibility effects.

3.1.3 Complex Geometry Handling and Meshing

The Lattice Boltzmann approach is solved on Cartesian meshes, which are generated automatically for any geometrically complex shape. Variable refinement regions (VR) can be defined to allow for local mesh refinement of the grid by successive factors of two. The position and size of the local refinement regions used here correspond to the previously published results by König et al [16]. An illustration of the computational mesh around the NASA-CRM installed in the ETW test section is given in Figure 3-1.

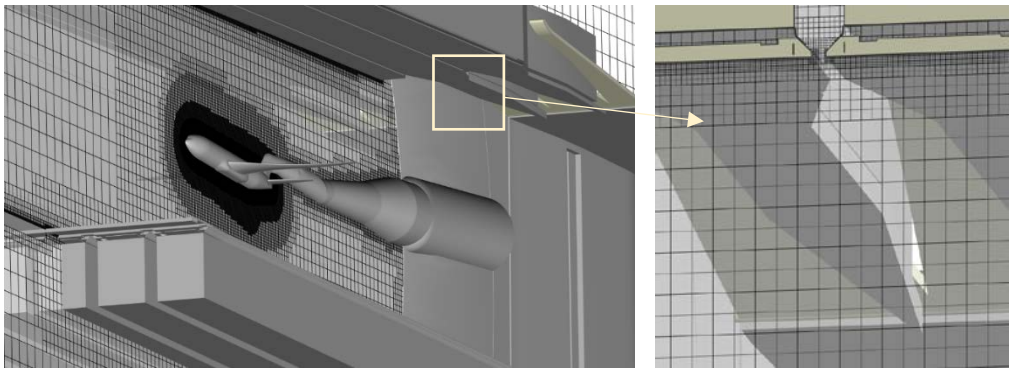

Figure 3-1: Illustration of the computational mesh around the NASA-CRM (coarsened for visualization) and in the slot/re-entry region (actual resolution).

3.2 Simulation Setup

Following the argumentation by Melber et al [30], the baseline simulation setup comprises the part of the wind tunnel starting from the stilling chamber, including nozzle and test section, and ends in this case behind the second throat and in front of the diffusor. The reason for including stilling chamber and nozzle in the simulation

is the lack of a priori information about the boundary layer and potential non-uniformities of the flow at the entrance to the test section. At the stilling chamber, where effectively no boundary layer is present after the flow straighteners, a well-defined numerical inlet boundary condition can be applied, prescribing total conditions for pressure and temperature. At the downstream end of the simulation domain, the natural position to apply a numerical boundary condition is after the second throat. When operated at Mach numbers between 0.7 and 1.0, the ETW is typically choked in the second throat to minimize the upstream propagation of disturbances from the drive system and to provide highly accurate Mach number control. Control of the flow velocity is then achieved by adjusting the mass flow adaptively through changing the throat area by means of flaps. To approximate this mechanism, the simulation modelled the second throat in wide open position and instead applied a static pressure outlet condition to drive and control the flow. For the current investigation, where sideslip and roll angles were zero, a symmetry condition was applied. Also, at the current stage of the investigation, fluid properties of air were used rather than those of nitrogen as it is used in the tunnel. The differences, however, are expected to be small for the current flow conditions. Results obtained using this baseline simulation setup will be presented in Section 4.1.

While this setup allows to use well-defined and simple numerical boundary conditions, it has one major disadvantage for the current work. Using the not a priori known static pressure at the exit p_{exit} to control the flow velocity inside the test section requires adaptive feedback control to achieve the desired Mach number with an accuracy of $\Delta M \approx \pm 0.001$. However, executing such a feedback control for the current setup poses the problem of vastly different time scales for the wind tunnel flow on the one side, and the local flow around the test article on the other side. Such large differences in time scales can lead to longer computational time for numerical schemes with explicit time integration.

3.2.1 Simulation Geometry

The geometry of the wind tunnel in the simulation provided as CAD files includes a heavily simplified representation of the actual plenum. This is deemed sufficient for this project as, by definition, the plenum should be treated as a large buffer vessel. More complex representations could easily be incorporated in the modelling if necessary. The mechanism to set the angle-of-attack, by means of rotating the support sting assembly carrying the aircraft model, is reproduced in the simulation setup, allowing easy and geometrically consistent changes of the model's incidence.

The NASA-CRM model is based on the baseline geometry with the original wing twist distribution as it was provided for the Sixth AIAA Drag Prediction Workshop [31]. To account for the aeroelastic deformations that the model experienced under wind-on conditions in the wind tunnel, the method described previously in [32] is employed to morph the wing shape according to the twist distributions measured in ETW. Linear interpolation of the deformations is applied for angles-of-attack within the range of the measured angles.

3.2.2 Timescales for Simulation

From previous work on the NASA-CRM configuration, documented in [16, 32], it is known that somewhere between 20-100 flow passes of the mean-aerodynamic-chord, depending on the flow condition, are sufficient to achieve a converged flow solution with the current numerical method. For the 2.7%-scale model of the NASA-CRM at M=0.85 this corresponds to a simulated physical time in the order of $t = 0.025s$. For the wind tunnel, however, the relevant timescales are in the order of $1 \ldots 10s$, about two orders of magnitude larger. To illustrate that, the Mach number response of a simplified two-dimensional model with similar characteristics to a step change in the exit pressure at $t = 1s$ is shown in Figure 3-2. From this, it can be seen that there is a lag time of about $\Theta_d = 0.15s$ before the first effect of that change is even seen at the reference point further upstream. The reason for that lag is the high Mach number that reduces the effective upstream pressure wave propagation velocity of the pressure change to as little as $\sim 50 \frac{m}{s}$. Then it takes the numerical model of the wind tunnel another $0.5s$ to settle to a new converged Mach number. The matter is further complicated by

pressure differences between the test section and the plenum that may occur while the tunnel flow settles. These pressure differences may lead to a net transfer of mass between test section and plenum. To achieve mass conservation of the test section flow therefore requires a sufficiently long settling time. Taking into account that this process needs to be repeated several times in an adaptive feedback loop illustrates why the timescales for the wind tunnel simulation are so much larger than for the test article. As a result, it requires a long physical time to simulate both the wind tunnel, as described above, and the test model in one monolithic simulation if accurate Mach number matching within the bounds mentioned above is required.

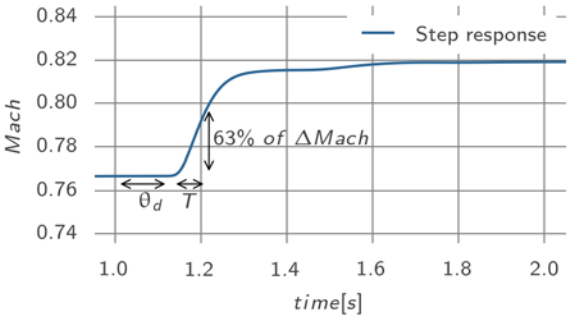

Figure 3-2: Mach number response of a simplified model to a step input in p_{exit}

The total simulation time can be reduced, if the timescale required by the wind tunnel flow to achieve the desired Mach number is shortened. One important step is to reduce the initial transient of the wind tunnel that is encountered when starting the tunnel up from zero velocity. This can be achieved by using a previous flow solution as initialization of the flow domain. All simulations presented here were seeded from a previous flow solution. In addition, a significant reduction in simulation time for the wind tunnel can be realized if the simulation setup is changed and boundary conditions with a more direct control over the Mach number are employed. To achieve that, a reduced simulation domain was set up with the stilling chamber and the nozzle removed. Instead, a velocity and pressure inlet is applied at the entrance to the test section. To solve the previously mentioned difficulty of the unknown velocity distribution at the entrance to the test section, distributions for all relevant flow quantities were extracted on the entrance plane from a previous simulation of the baseline wind tunnel setup with nozzle that had achieved a very similar Mach number. Scaling the resulting distributions by employing isentropic relations allows to directly set the flow conditions in the wind tunnel to the exact Mach number targeted, without the need for a time-consuming iteration process. Illustrations of the baseline and the reduced simulation setups are shown in Figure 3-3.

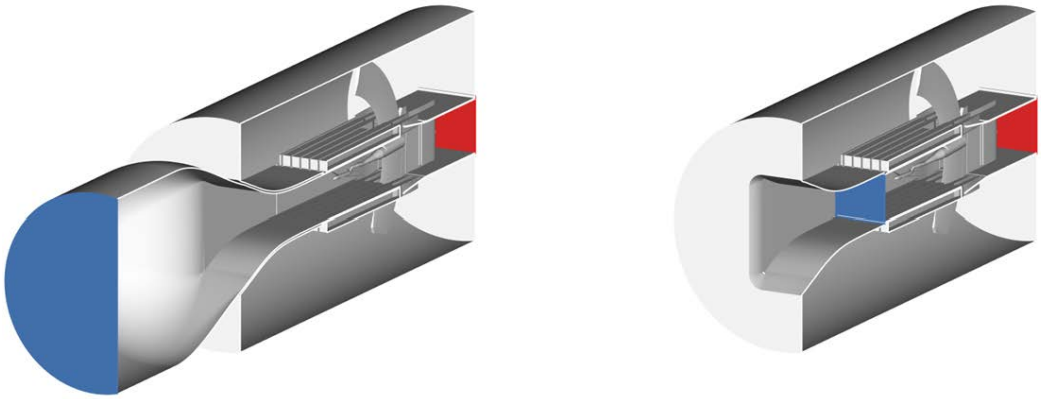

Figure 3-3: Illustrations of the baseline (left) and the reduced wind tunnel simulation setups. The regions where numerical inlet and outlet boundary conditions are applied are highlighted in blue and red, respectively.

Quantitative comparisons to experimental results for the baseline and the reduced setup are presented in Sections 4.1 and 4.2, respectively.

3.2.3 Reference Conditions

For a consistent definition of the reference Mach number M_{ref} in both the simulation and the experiments, it is derived in the simulations in a way mimicking the method used in the actual ETW. The reference static pressure p_{ref} is measured at the tunnel sidewall at $x = 746\,mm$ downstream from the test section entrance. Using the total pressure p_t in the flow, the Mach number can be derived from the isentropic relation:

$$M_{\text{ref}} = \sqrt{\frac{\left(\left(\frac{p_t}{p_{\text{ref}}}\right)^{\frac{\gamma-1}{\gamma}} - 1\right)}{\frac{\gamma-1}{2}}}$$

It is worthwhile to note that the reference Mach number derived using this definition differs from the average value measured directly in the flow at the same streamwise location in that it is typically slightly lower.

For the simulation cases with a reduced domain, i.e. where the nozzle and stilling chamber were replaced by an inlet boundary condition, the reference total pressure p_t is measured as the average value at the test section center, outside of the wall boundary layers. It was verified that the measured value at that location is within 0.1% of the reference value in the stilling chamber.

The reference static pressure p_{ref} as it was measured in the simulation was also used to normalize the coefficients for pressure, forces and moments presented further below

4.0 RESULTS

In this section, simulation results will be compared quantitatively to experimental results obtained at ETW during the ESWIRP [33] test campaign. ETW data is linearly interpolated to match the Mach number achieved in the respective simulation. For example, for a simulation run that reached a reference Mach number of M=0.865, experimental reference data was interpolated between the ETW polar runs 156 and 157 for M=0.86 and 0.87, respectively. This interpolation does not take into account the non-linear behaviour of the flow in transonic conditions, but the result is still expected to be more representative than the non-interpolated source data due to the small variation in Mach number.

4.1 Full Simulation Domain

Some simulations were conducted including the full simulation domain as discussed above, i.e. including the stilling chamber and the nozzle. For those runs, the computational effort required to match the exact tunnel flow conditions, in particular the Mach number, without employing the aforementioned acceleration techniques becomes large. However, it was deemed necessary to perform such simulations to obtain reference solutions against which the more efficient future runs can be verified. The computational cost was limited here by allowing a larger difference to the targeted Mach number. The result presented here was iterated until a reference Mach number of M=0.865 was achieved for an angle-of-attack of $\alpha = 3.0°$.

To give an impression of the relevant flow features related to the slots in the simulation, distributions of the vertical velocity in a y-plane are shown in Figure 4-1. Note that in those images the model is installed in an upright attitude, whereas the wind tunnel tests are usually done inverted. The left image shows an overview of the simulation domain with the normalized z-velocity w/U_∞ in a plane cutting through the outboard wing of the NASA-CRM model and through one of the slots in the tunnel floor and ceiling. The middle image gives a close-up of the instantaneous flow in the test section area, whereas the image on the right side shows the time averaged flow velocities. It is interesting to note that, while on average the flow is clearly entering from the plenum in the front part of the test section, the instantaneous view reveals that the slot flow is actually

dominated by a series of vortices travelling downstream along the slot. Towards the rear end of the test section, in the re-entry zone, the local velocity directions seem to indicate that the flow is in fact leaving the test section. This is, however, misleading as the flow in the region of the finger-flaps is dominated by longitudinal vortices and the plane presented here is cutting through the center of such a vortex pair. Overall, the slot flow seems vortex dominated and highly unsteady and those structures will be investigated in more detail in future work.

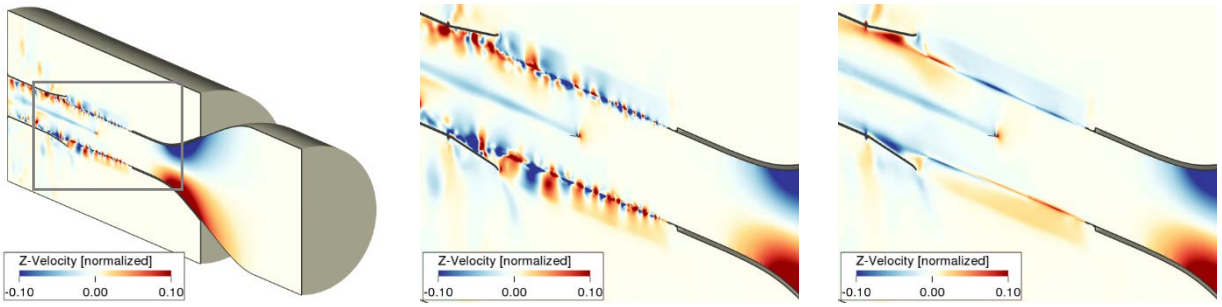

a – Instantaneous (full view) | **b - Instantaneous (close-up)** | **c - time-averaged (close-up)**

Figure 4-1: Distribution of vertical velocity (normalized with reference velocity) in a plane with y=0.645m; instantaneous snap-shots and time-averaged view. Flow is from right to left.

To further highlight the unsteadiness of the flow, histories for lift and pitching moment coefficients are shown in Figure 4-2. The simulation was initialized using a prior simulation and, hence, the time histories don't show the highly transient start-up behaviour of the wind tunnel simulation. Instead, flow conditions were already very close to the final conditions and hence there is only a very mild initial transient over approximately the first $0.05s$. After that, both histories for C_L and C_{My} exhibit sustained oscillations around a statistically converged mean value. The results presented here for this simulation are based on a time averaged solution starting from $t = 0.05s$, highlighted in the C_L and C_{My} plots.

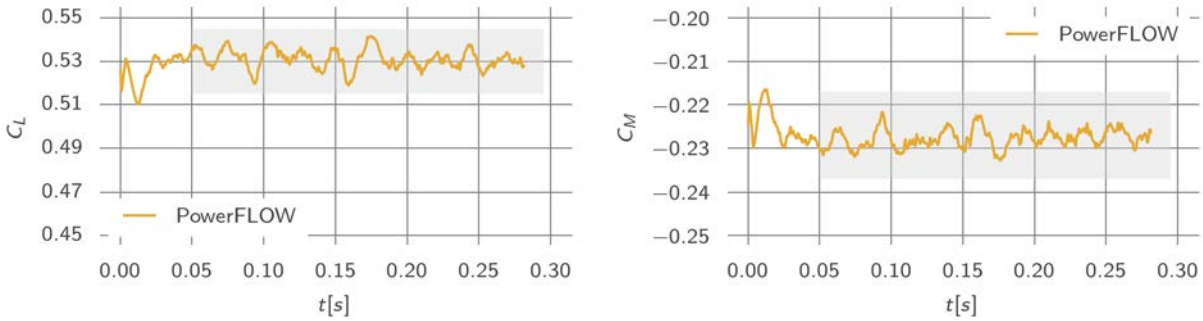

Figure 4-2: Time histories of lift and pitching moment at M=0.865, α=3.0 in the complete test section + nozzle simulation.

To quantitatively compare the simulation to experimental results, a series of wall pressure signatures from the test section are presented. The positions of the pressure measurement lines inside the test section are illustrated in Figure 4-3, with the sections high-lighted in red colour for which data is shown here. The pressure distributions are shown in Figure 4-4.

The sections denoted ‘TBL’ here represent the horizontal wall facing the models suction side and ‘TIL’ corresponds to one of the side walls. The test section entrance is located at $x = 0\ m$ and the test article is placed in the range $x = 3 \ldots 4\ m$. All four pressure distributions presented here show a good agreement between simulations and experimental results. Overall pressure gradients along the test section are captured as well as the model’s signature. Some deviations exist in the region of the adverse pressure gradient downstream of the model, which are subject to further investigation. In general, the agreement is sufficiently good to give confidence that the method presented here is capable to capture the effect of the model on the wall pressure distributions, and thereby also the reciprocal effect of the walls on the model.

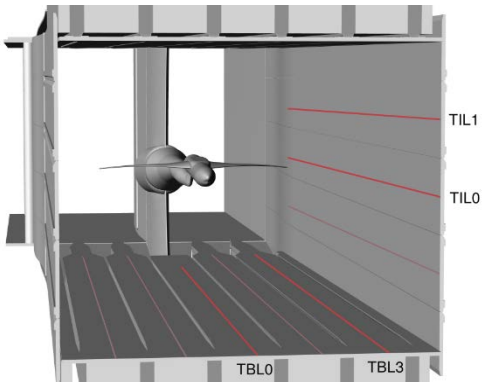

Figure 4-3: Illustration of the wall pressure positions (CRM orientation upside-down)

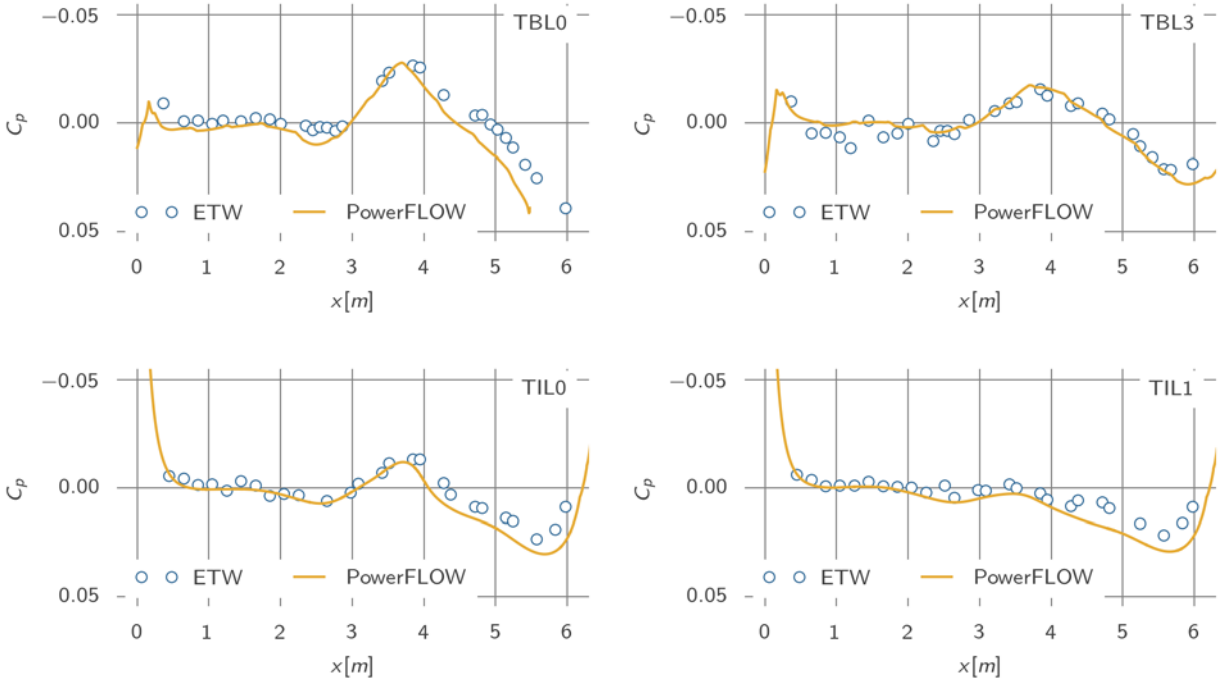

Figure 4-4: Wall pressure distributions at M=0.865, α=3.0°, (top row: model suction side, bottom row: side wall) in the complete test section + nozzle simulation. (ETW data interpolated from polars 156 and 157)

Selected wing pressure distributions at $M = 0.865$ and $\alpha = 3.0°$ are shown in Figure 4-5. Again, the simulation results correlate well to the experimental data. Some discrepancies on the two outboard sections presented are in line with the overall trends seen at the Drag Prediction Workshop, where the CFD solutions tended to predict a shock location further downstream than the experiments. The fact that a similar trend is encountered here may suggest that the reason for this offset in shock location is not related to wall interferences in the wind tunnel. It is, however, too early to draw final conclusions on this and further investigations will follow. In principal, the comparison shows that the simulation is able to capture the flow around the NASA-CRM model correctly in installed conditions.

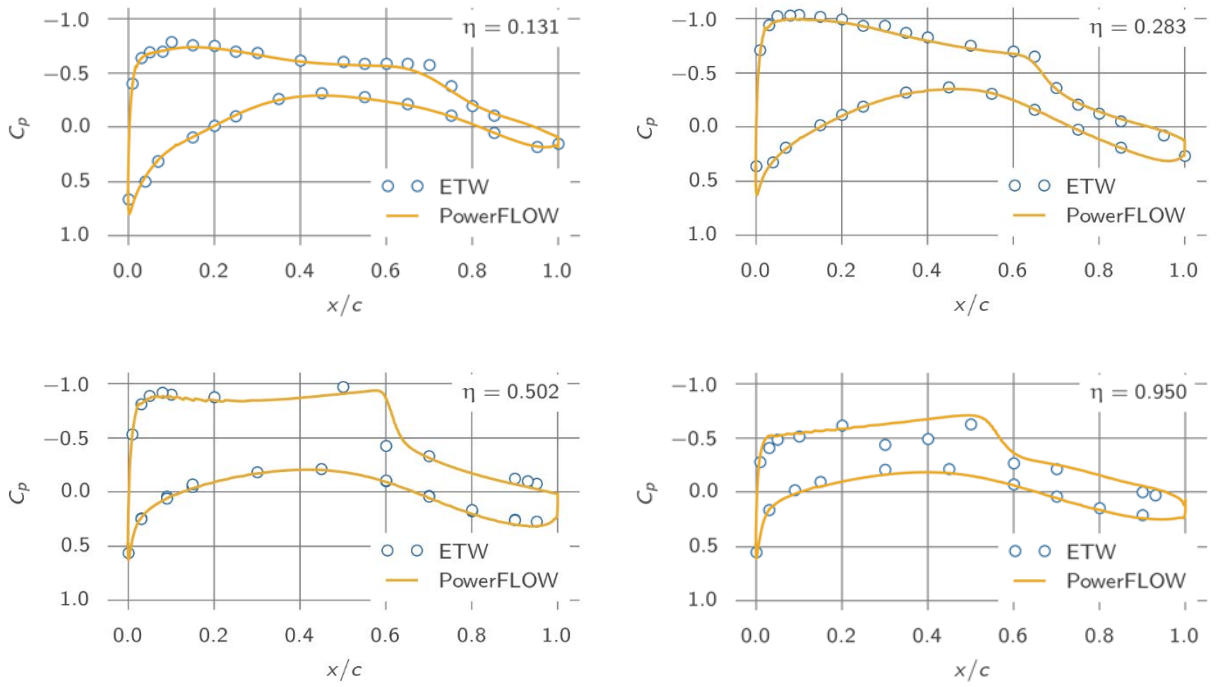

Figure 4-5: NASA-CRM wing section pressure distributions at M=0.865, α=3.0°, in the complete test section + nozzle simulation. (ETW data interpolated from polars 156 and 157)

4.2 Reduced Simulation Domain

To improve the matching of the Mach number to the desired conditions and to speed-up the overall simulation, a number of simulations were conducted using the reduced setup that replaces the nozzle with an inlet boundary condition at the entrance to the test section. Results of these simulations are presented in this section. Several angles-of-attack were simulated within the design range, but also deep in the aircraft's buffet range.

A comparison of integrated coefficients for lift, drag and pitching moment is presented in Figure 4-6. Again, experimental ETW results are interpolated to the actual reference Mach number achieved in the simulations, which was here $M = 0.8521$. The limited number of simulation results available at the time of writing indicate that the polar shapes are very well matched. Even at the highest angle-of-attack, where the flow is highly unsteady and with large separations due to shock buffet on the wing, the agreement is reasonably good. The larger over-prediction of lift in that range is related to a delayed onset of buffet on the inboard wing in the simulation, as will be shown further down. But overall, the behaviour is in line with previous buffet investigations performed in free-air conditions and published in [34, 16]. It is interesting to note that the simulations here show similar trends with regards to the experiments as have been observed previously in free-air simulations. Especially the systematic over-prediction of lift and the more nose-down pitching moment from CFD have been discussed in the context of the Sixth Drag Prediction Workshop [35]. The fact that those discrepancies persist in the wind tunnel simulations presented here indicates that either the simulations are not able to capture all wind tunnel effects, or that those discrepancies are related to other differences between the NASA-CRM model as it was built and tested in the wind tunnel, and the numerical model employed by the CFD simulations. The first option is currently being investigated in that it is an important aspect of the ongoing validation work presented here.

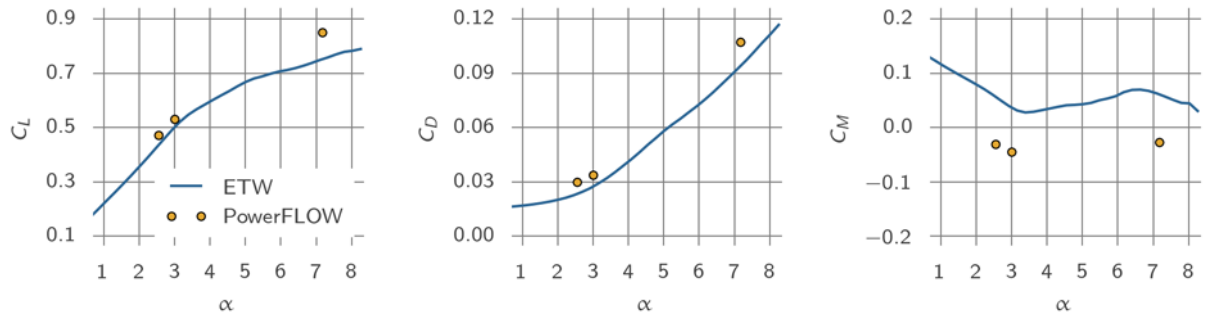

Figure 4-6: Integrated forces and pitching moment for the reduced wind tunnel setup at M=0.852.

A comparison of selected wing pressure distributions is shown in Figure 4-7 for the reduced setup. Here, results for a moderate and a high angle-of-attack, $\alpha = 3.0°$ and 7.17°, are presented. At $\alpha = 3.0°$, the simulation pressure distributions correlate very well with the experimental measurements. Only the outboard wing, shown here at $\eta = 0.950$, exhibits a slightly different shock structure. Again, this is an indication that either some effect is missing in the modelling of the wind tunnel, or that the numerical model of the NASA-CRM differs from the actually built model for the wind tunnel test. For the higher angle-of-attack of $\alpha = 7.17°$, which features massively separated flow and unsteady shock movements, there is a certain mismatch on the inboard wing at $\eta = 0.283$, where the transonic buffet with its trailing edge separation is already visible in the experiments, but not in the simulation. Further outboard, however, the agreement is again good, especially when taking the extreme flow conditions into account. The delayed separation on the inboard wing also explains the over-prediction of lift seen in Figure 4-6.

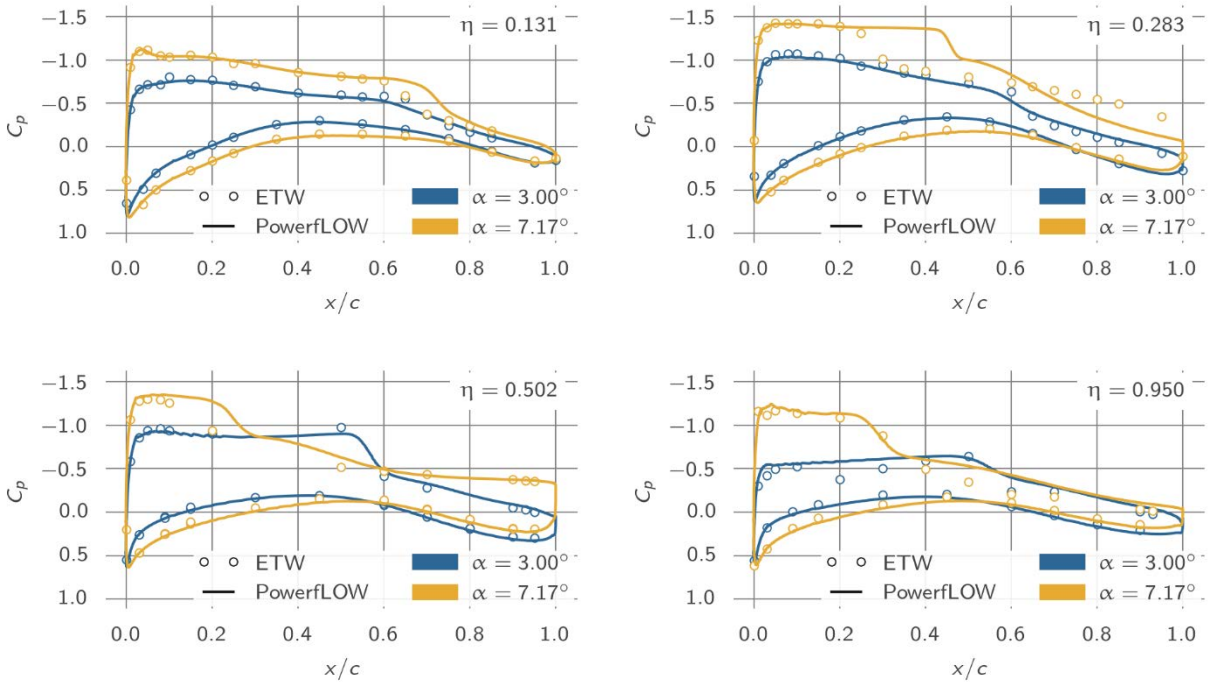

Figure 4-7: NASA-CRM wing section pressure distributions at M=0.852, α=3.0° and 7.17°, in the reduced simulation without nozzle. (ETW data interpolated from polars 153 and 155)

The agreement of the pressure distributions is again overall good. It confirms that replacing the nozzle in the simulation by an inlet boundary condition with similar distribution of the flow quantities is a viable approach to reduce the overall computational effort while maintaining good correlation to the actual experimental wind tunnel flow.

Finally, the sensitivity of the wall pressure distributions to changes of angle-of-attack is shown in Figure 4-8. Again, $\alpha = 3.0°$ and $7.17°$ are compared and both the absolute agreement to experiments as well as the incremental effect of the angle-of-attack change are well reproduced. This gives confidence that the current method accurately captures the wind tunnel installation effect and can be used to support the assessment of wind tunnel corrections.

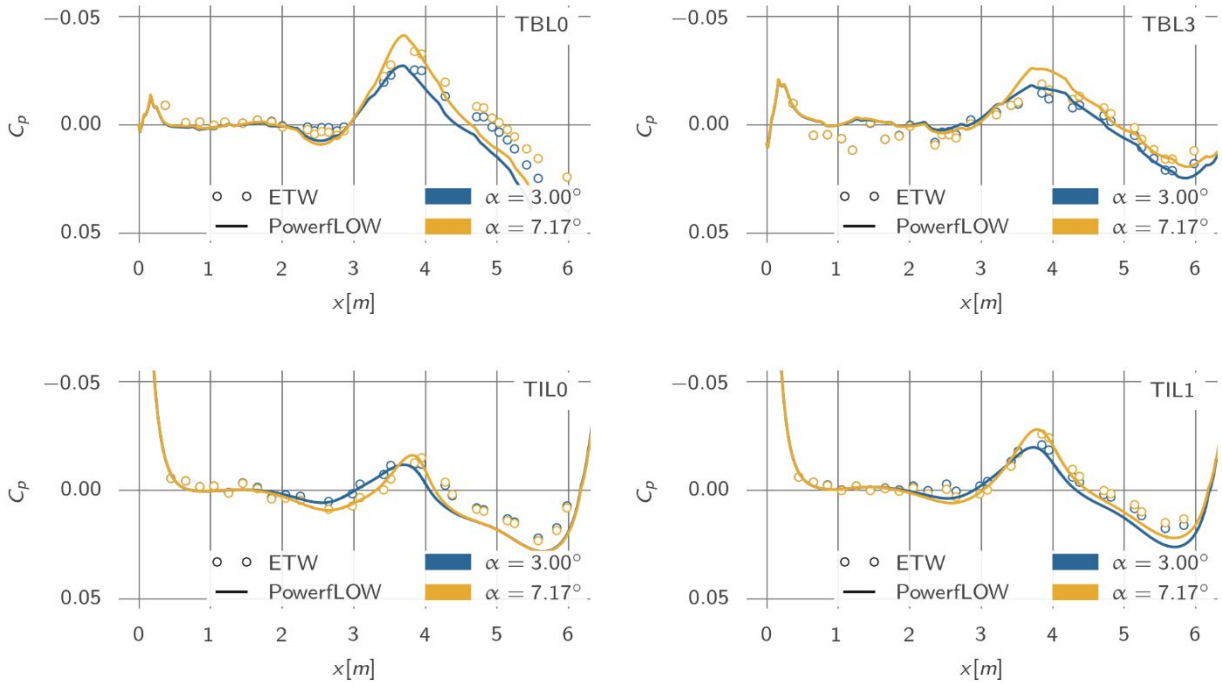

Figure 4-8: Wall pressure distributions at M=0.852, α=3.0° and 7.17°, (top row: model suction side, bottom row: side wall) in the reduced simulation without nozzle. (ETW data interpolated from polars 153 and 155)

5.0 SUMMARY AND CONCLUSIONS

An unsteady transonic Lattice Boltzmann method is used to simulate the slotted wall test section of the European Transonic Windtunnel. Measurements performed on the NASA Common Research Model are used to validate the simulation results.

The full simulation domain includes the slotted wall test section with plenum and the nozzle with stilling chamber. It is discussed that this setup allows for well-defined numerical boundary conditions, but at the same time poses problems to efficiently converge both the global flow conditions in the tunnel and the local flow around the test article. Simulation strategies are briefly discussed to reduce the overall computational cost. One such strategy is to use a previous simulation of the complete domain to derive boundary conditions for subsequent simulations with a reduced computational domain. A limited number of validation results for the complete simulation domain as well as for a reduced setup are presented and compared to experimental results. Good agreement, especially of the wall pressure distributions, was achieved, even at high angles-of-attack.

This gives confidence that the numerical method can be used to assess and extend the wind tunnel interference corrections at extreme flow conditions and can help to understand the pertinent flow interactions. The current work thereby merely represents a first step towards a more detailed validation and investigation. Further validation studies and process optimizations, to allow more efficient simulations and better matching of the target flow conditions, are currently ongoing.

Bibliography

[1] A. Hashimoto and M. Kohzai, "Wall Interference Analysis by Whole Wind Tunnel CFD," in *5th Symposium on Integrating CFD and Experiments in Aerodynamics*, 2012.

[2] W. C. Schuman, "A Computational Evaluation of Transonic Wind Tunnel Wall Interference on High Aspect Ratio Models in the Arnold Engineering Development Complex 16 Foot Transonic Tunnel.," University of Tennessee, 2016.

[3] B. Goffert, M. A. Ortega and J. B. P. F. Filho, "Numerical Study of Wall Ventilation in a Transonic Wind Tunnel," *Journal of Aerospace Technology and Management*, vol. 7, pp. 81-92, 2015.

[4] J. E. J. Maseland, M. Laban, H. Ven and J. W. Kooi, "Development of CFD-based interference models for the DNW-HST transonic wind tunnel," National Aerospace Laboratory NLR, NLR-TP-2006-504, 2006.

[5] I. A. Kursakov, A. R. Gorbushin, S. M. Bosnyakov, S. A. Glazkov, A. V. Lysenkov, S. V. Matyash, A. V. Semenov and J. Quest, "A numerical approach for assessing slotted wall interference using the CRM model at ETW," *CEAS Aeronautical Journal*, p. 1–20, 2017.

[6] J. Slotnick, A. Khodadoust, J. Alonso, D. Darmofal, W. Gropp, E. Lurie and D. Mavriplis, "CFD Vision 2030 Study: A Path to Revolutionary Computational Aerosciences," NASA/CR-2014-218178, 2014.

[7] ETW GmbH, "ETW - User Guide," 2004.

[8] S. Succi, The Lattice Boltzmann Equation for Fluid Dynamics and Beyond, Oxford University Press, 2001.

[9] H. Chen, C. Teixeira and K. Molvig, "Realization of Fluid Boundary Conditions via Discrete Boltzmann Dynamics," *International Journal of Modern Physics C*, vol. 09, pp. 1281-1292, 1998.

[10] H. Chen, S. Kandasamy, S. Orszag, R. Shock, S. Succi and V. Yakhot, "Extended Boltzmann Kinetic Equation for Turbulent Flows," *Science*, vol. 301, pp. 633-636, 2003.

[11] S. Chen and G. D. Doolen, "Lattice Boltzmann Method for Fluid Flows," *Annual Review of Fluid Mechanics*, vol. 30, pp. 329-364, 1998.

[12] H. Chen, S. Chen and W. H. Matthaeus, "Recovery of the Navier-Stokes equations using a lattice-gas Boltzmann method," *Physical Review A*, vol. 45, pp. R5339-R5342, 1992.

[13] Y. Qian, D. d'Humieres and P. Lallemand, "Lattice BGK Models for the Navier-Stokes Equation," *Europhysics Letters*, vol. 17, pp. 479-484, 1992.

[14] A. F. P. Ribeiro, D. Casalino, E. Fares and M. Choudhari, "Direct Numerical Simulation of an Airfoil with Sand Grain Roughness on the Leading Edge," NASA/TM-2016-219363, 2016.

[15] B. König, E. Fares, M. Murayama, Y. Ito, Y. Yokokawa, K. Yamamoto and K. Ishikawa, "Lattice-Boltzmann Simulations of the JAXA JSM High-Lift Configuration," in *34th AIAA Applied Aerodynamics Conference*, AIAA 2016-3721, 2016.

[16] B. König and E. Fares, "Exa PowerFLOW Simulations for the Sixth AIAA Drag Prediction Workshop," *Journal of Aircraft*, 2018, doi: 10.2514/1.C034480.

[17] E. Fares, B. Duda and M. R. Khorrami, "Airframe Noise Prediction of a Full Aircraft in Model and Full Scale Using a Lattice Boltzmann Approach," in *22nd AIAA/CEAS Aeroacoustics Conference*, AIAA 2016-2707, 2016.

[18] M. R. Khorrami, E. Fares and D. Casalino, "Towards Full Aircraft Airframe Noise Prediction: Lattice Boltzmann Simulations," in *20th AIAA/CEAS Aeroacoustics Conference*, AIAA 2014-2481, 2014.

[19] B. König, E. Fares, P. Ravetta and M. R. Khorrami, "A Comparative Study of Simulated and Measured Main Landing Gear Noise for Large Civil Transports," in *23rd AIAA/CEAS Aeroacoustics Conference*, AIAA 2017-3013, 2017.

[20] R. Zhang, X. Shan and H. Chen, "Efficient kinetic method for fluid simulation beyond the Navier-Stokes equation," *Physical Review E*, vol. 74, no. 4, p. 046703, 10 2006.

[21] H. Chen, I. Goldhirsch and S. A. Orszag, "Discrete Rotational Symmetry, Moment Isotropy, and Higher Order Lattice Boltzmann Models," *Journal of Scientific Computing*, vol. 34, pp. 87-112, 1 2008.

[22] H. Chen and X. Shan, "Fundamental conditions for N-th-order accurate lattice Boltzmann models," *Physica D: Nonlinear Phenomena*, vol. 237, pp. 2003-2008, 8 2008.

[23] X. Shan, X.-F. Yuan and H. Chen, "Kinetic theory representation of hydrodynamics: a way beyond the Navier Stokes equation," *Journal of Fluid Mechanics*, vol. 550, pp. 413-441, 2006.

[24] E. Fares, M. Wessels, Y. Li, P. Gopalakrishnan, R. Zhang, C. Sun, N. Gopalaswamy, P. Roberts, J. Hoch and H. Chen, "Validation of a Lattice-Boltzmann Approach for Transonic and Supersonic Flow Simulations," in *52nd Aerospace Sciences Meeting*, AIAA 2014-0952, 2014.

[25] V. Yakhot and S. A. Orszag, "Renormalization Group Analysis of Turbulence. I. Basic Theory," *Journal of Scientific Computing*, vol. 1, pp. 3-51, 1986.

[26] H. Chen, S. Orszag, I. Staroselsky and S. Succi, "Expanded analogy between Boltzmann Kinetic Theory of Fluid and Turbulence," *Journal of Fluid Mechanics*, vol. 519, pp. 307-314, 2004.

[27] F. Menter, M. Kuntz and R. Bender, "A Scale-Adaptive Simulation Model for Turbulent Flow Predictions," in *41st Aerospace Sciences Meeting and Exhibit*, AIAA 2003-767, 2003.

[28] H. Chen, "Volumetric formulation of the lattice Boltzmann method for fluid dynamics: Basic concept," *Physical Review E*, vol. 58, pp. 3955-3963, 1998.

[29] A. Anagnost, A. Alajbegovic, H. Chen, D. Hill, C. Teixeira and K. Molvig, "Digital Physics Analysis of the Morel Body in Ground Proximity," in *SAE International Congress and Exposition*, SAE Technical Paper 970139, 1997.

[30] S. Melber-Wilkending and G. Wichmann, "Application of Advanced CFD Tools for High Reynolds Number Testing," in *47th AIAA Aerospace Sciences Meeting*, AIAA 2009-418, 2009.

[31] *6th AIAA CFD Drag Prediction Workshop.*

[32] B. König and E. Fares, "Validation of a Transonic Lattice-Boltzmann Method on the NASA Common Research Model," in *54th AIAA Aerospace Sciences Meeting*, AIAA 2016-2023, 2016.

[33] European Strategic Wind tunnels Improved Research Potential (ESWIRP), "The ESWIRP ETW TNA test results," [Online]. Available: http://www.eswirp.eu/ETW-TNA-Dissemination.html. [Accessed 15 March 2015].

[34] A. F. Ribeiro, B. König, D. Singh, E. Fares, R. Zhang, P. Gopalakrishnan, A. Jammalamadaka, Y. Li and H. Chen, "Buffet Simulations with a Lattice-Boltzmann based Transonic Solver," in *55th AIAA Aerospace Sciences Meeting*, AIAA 2017-1438, 2017.

[35] E. N. Tinoco, O. Brodersen, S. Keye, K. Laflin, E. Feltrop, J. C. Vassberg, M. Mani, B. Rider, R. A. Wahls, J. H. Morrison, D. Hue, M. Gariepy, C. J. Roy, D. J. Mavriplis and M. Murayama, "Summary of Data from the Sixth AIAA CFD Drag Prediction Workshop: CRM Cases 2 to 5," in *55th AIAA Aerospace Sciences Meeting, AIAA SciTech Forum*, AIAA 2017-1208, 2017.